

Doublon production in correlated materials by multiple ion impacts

Lotte Borkowski,¹ Niclas Schlünzen,¹ Jan Philip Joost,¹ Franziska Reiser,¹ and Michael Bonitz¹

¹*Institut für Theoretische Physik und Astrophysik, Christian-Albrechts-Universität zu Kiel, Leibnizstrasse 15, 24098, Kiel, Germany*

In a recent Letter [Balzer *et al.*, Phys. Rev. Lett. **121**, 267602 (2018)] it was demonstrated that ions impacting a correlated graphene cluster can excite strongly nonequilibrium states. In particular, this can lead to an enhanced population of bound pairs of electrons with opposite spin — doublons — where the doublon number can be increased via multiple ion impacts. These predictions were made based on nonequilibrium Green functions (NEGF) simulations allowing for a time-dependent non-perturbative study of the energy loss of charged particles penetrating a strongly correlated system. Here we extend these simulations to larger clusters and longer simulation times, utilizing the recently developed G1–G2 scheme [Schlünzen *et al.*, Phys. Rev. Lett. **124**, 076601 (2020)] which allows for a dramatic speedup of NEGF simulations. Furthermore, we investigate the dependence of the energy and doublon number on the time interval between ion impacts and on the impact point.

PACS numbers: 05.30.-d, 34.10.+x, 34.50.Bw, 71.10.Fd

I. INTRODUCTION

The interaction of charged particles with matter is of high relevance for many areas of physics and astrophysics. Processes such as the stopping power or stopping range of projectiles in matter allow one to analyze their energy spectrum. On the other hand, the energy loss of charged particles in matter is a sensitive tool to diagnose the electronic properties of the material. In soft collisions of heavy charged particles, such as ions, with a solid, typically the electrostatic force, i.e., the Coulomb interaction, has the largest impact, leading to excitation and ionization of electrons in the target material and, thus, to the loss of kinetic energy of the projectile [1]. For nonrelativistic projectile velocities of the order of or larger than the Fermi velocity ($\sim 10^6$ m/s in metals), theoretical approaches based on scattering theory [2] or on the linear response functions of the uniform electron gas [3] provide an accurate description of the energy transferred during the collision process. However, they neglect the precise atomic composition of the target, electronic correlations, as well as nonlinear effects [4, 5].

In the same velocity regime, recent theoretical progress is due to time-dependent density functional theory (TDDFT), which has been applied to describe the slowing down of charged particles in a variety of solids, including metals [6–8], semimetals [9, 10] and clusters [11, 12], narrow-band-gap semiconductors [13], insulators [14, 15] and monolayer systems such as graphene, e.g. Ref. [16]. Taking into account primarily the excitation of valence electrons, these simulations yield satisfactory results for the electronic stopping power (the transfer of energy to the electronic degrees of freedom per unit length traveled by the projectile) and work for a wide range of impact energies. On the other hand, a rather general tool to determine the stopping power of energetic ions in matter is provided by the SRIM code [17], which uses the binary collision approximation in combination with an averaging over a large range of experimental situations, and data being available for many materials and gaseous targets. At the same time, linear response, TDDFT and SRIM have difficulties in accounting for strong electron-electron correlations which are crucial, e.g., in transition metal oxides [18] or spe-

cific organic materials [19]. In addition, we note that SRIM and linear response theory do not account for time-dependent changes in the target during the collision process, which limits their applicability.

For this reason we have developed an alternative approach to the stopping power that is based on nonequilibrium Green functions (NEGF) [20–23]. This method allows one to systematically include electron-electron correlations via a time-dependent many-body selfenergy, and it has recently successfully been applied to strongly correlated lattice systems as well [24, 25]. Particular advantages of the NEGF approach are that it is not limited to either weak or strong coupling and that it is particularly well suited to study finite-sized clusters and spatially inhomogeneous systems on a self-consistent footing. Recently, NEGF simulations coupled to an Ehrenfest dynamics of the projectile were developed [26], and good agreement with TDDFT and SRIM simulations was established. A particular interesting result of NEGF simulations in the low velocity range was the prediction of a non-trivial electronic correlation effect: the formation of doublons, i.e. bound pairs of electrons with opposite spin, as a result of ion impact. In a recent Letter [27] it was demonstrated that the doublon number can be further increased if the material is hit by multiple ions. This issue was further explored in Refs. [28, 29]. Another important issue during the impact of ions on solid targets is the possible transfer of charge to the ion (neutralization) which has been studied in a number of experiments, e.g. Refs. [30, 31]. A first attempt to extend the NEGF-Ehrenfest approach to include charge exchange processes has been made in Ref. [32].

On the other hand, the NEGF approach is computationally very demanding. While in recent years efficient numerical schemes have been developed to solve the underlying Keldysh–Kadanoff–Baym equations (KBE) [22, 33–39], the solution is hampered by a cubic scaling of the CPU time with the number of time steps N_t . This scaling can be reduced to quadratic by applying the generalized Kadanoff–Baym ansatz (HF-GKBA). Recently we could show that even linear scaling can be achieved if the HF-GKBA is rewritten as a coupled system of time-local equations for the one- and two-particle Green function which was called “G1–G2 scheme” [40].

In the present paper we take advantage of the speedup provided by the G1–G2 scheme to significantly extend the previous stopping simulations for multiple ion impacts of Ref. [27]. We study significantly larger hexagonal monolayer clusters of up to 96 sites, extend the simulation duration, and study how the excitation by the ion propagates through the cluster. Further, we vary the time interval between successive ion impacts as well as the impact point and investigate how this influences the energy of the electrons and the doublon production. For short time intervals between impacts we are able to analyze non-adiabatic response effects where the effect of two projectiles does not simply add up because the cluster is driven far away from equilibrium. In addition to the long-range Coulomb interaction between cluster electrons and projectile we also consider a simpler model where the effect of the projectile is mimicked by a variation of the lattice potential. This scenario is of interest as well as it is easily realized for cold atoms in an optical lattice.

The paper is organized as follows. In Sec. II, we define the model Hamiltonian and introduce our NEGF approach as well as the G1–G2 scheme. In Sec. III, we present the simulation results. We conclude the paper with Sec. IV, outlining possible future work.

II. THEORY

A. Hubbard model for finite graphene clusters

To study the stopping dynamics of a classical charged particle which passes through a correlated system, we consider a finite lattice of electrons described by a single-band Fermi–Hubbard model and compute the energy exchange between projectile and cluster during the collision process. Details of the model are described in Ref. [26]. Here we only summarize the main points. The lattice as a whole is electrically neutral, i.e., the electronic charges are compensated by corresponding opposite charges located at the site coordinates \mathbf{R}_i . The energy exchange occurs via the Coulomb potential between the projectile, the fixed background charges and the target electrons which are initially in equilibrium. As the projectile we consider positively charged ions. When they approach the lattice they induce a confinement potential to the electrons which initiates a nonequilibrium electron dynamics.

As a target, we consider circular honeycomb clusters in the xy -plane with a finite number of honeycombs and a total of L sites, see Fig. 1 for an illustration. We focus on a half-filled system in the paramagnetic phase and use a lattice spacing of $a_0 = 1.42 \text{ \AA}$, which corresponds to the carbon-carbon bond length in graphene [41]. Using a nearest neighbor-hopping J and an on-site Hubbard repulsion U (which we consider time-dependent to account for adiabatic-switching procedures [23]), the Hamiltonian for the lattice electrons is

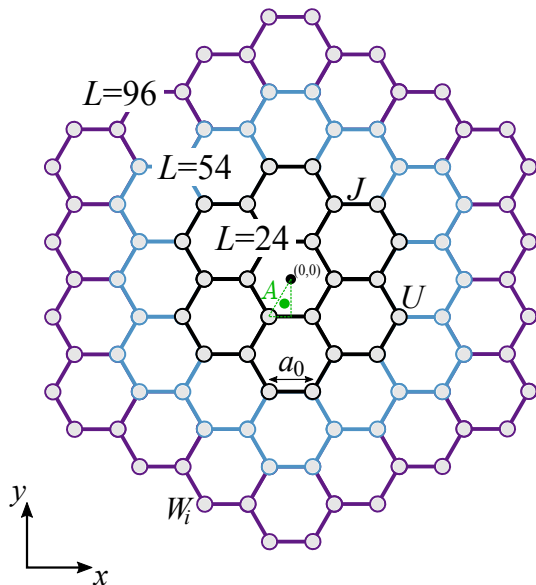


FIG. 1. Lattice structure of circular honeycomb clusters with $L = 24$ (black), 54 (blue) and 96 (purple) sites. The green point $A = \left(-\frac{1}{6}a_0, -\frac{\sqrt{3}}{3}a_0, 0\right)$ indicates the position where the projectile hits the lattice plane. Furthermore, $a_0 = 1.42 \text{ \AA}$ denotes the lattice spacing, $J = 2.8 \text{ eV}$ is the nearest-neighbor hopping, U the on-site interaction, and W_i is the time-dependent local energy produced by the projectile, cf. Eq. (2).

then given by

$$H_e(t) = -J \sum_{\langle i,j \rangle, \sigma} \hat{c}_{i\sigma}^\dagger \hat{c}_{j\sigma} + U(t) \sum_i \hat{n}_i^\uparrow \hat{n}_i^\downarrow + \sum_{i,\sigma} W_i(t) \hat{c}_{i\sigma}^\dagger \hat{c}_{i\sigma}, \quad (1)$$

where the operator $\hat{c}_{i\sigma}^\dagger$ ($\hat{c}_{i\sigma}$) creates (annihilates) an electron with spin σ on site i . Further, $\hat{n}_{i\sigma} = \hat{c}_{i\sigma}^\dagger \hat{c}_{i\sigma}$ and W_i denote the electron density operator and the external potential produced by the projectile, respectively.

For convenience, we measure J and U in electron volts, define U/J as the interaction strength for the electrons and use $t_0 = \hbar/J$ as the unit of time. Unless otherwise stated, we use $J = 2.8 \text{ eV}$ which is typical for graphene [42] and corresponds to $t_0 = 0.235 \text{ fs}$.

B. Incident-ion potential

We consider two different models to describe the time-dependent potential induced by the energetic ions. In the first scenario, we compute the classical **Coulomb** potential of incident ions of charge Z_p ,

$$W_i(t) = -\frac{e^2}{4\pi\epsilon_0} \frac{Z_p}{|\mathbf{r}_p(t) - \mathbf{R}_i|}, \quad (2)$$

where $\mathbf{r}_p(t)$ denotes the time-dependent position of the projectile, $-e$ is the electron charge and ϵ_0 the vacuum permittivity. In analogy to previous studies [26, 29], we set the initial position of the incident ion to $\mathbf{r}_p(0) = \left(-\frac{1}{6}a_0, -\frac{\sqrt{3}}{3}a_0, -z\right)$, see the centroid point of the green dashed triangle in Fig. 1. These coordinates have been found to give similar stopping results for the highly symmetric honeycomb lattice compared to calculations, where one averages over many different collision sites. The influence of the impact point will be studied separately in Sec. III F. Furthermore, the initial z -position is chosen such that the measured energy transfer becomes independent of the initial conditions (typically $z \gtrsim 10a_0$). The dependence of the energy exchange on the impact velocity was investigated in detail in Refs. [26, 27]. Here we are interested in the response of the target electrons to a varying number of projectiles. To this end we fix the ion velocity to a value $v_{p,0} = 3a_0/t_0 \approx 1.8 \cdot 10^6 m/s$ in z -direction, cf. Eq. (21). This is a comparatively large value close to the maximum of the stopping curve. The corresponding kinetic energy of the projectile is much larger than the energy exchanged with the target. Therefore, a selfconsistent solution of Newton's equation for the projectile can be avoided for all cases considered in this paper.

It is often useful to simplify the general Coulomb potential to investigate local effects induced by the excitation. For such applications, a short-ranged localized potential that excites a specific lattice site provides a reasonable approximation [27]. We will use a **Gaussian**,

$$W_i(t) = -W_0 \delta_{i,i_0} \exp\left(-\frac{t^2}{2\tau^2}\right), \quad (3)$$

with the amplitude W_0 , the excited lattice site i_0 (which we choose on the innermost honeycomb ring), and the interaction duration $\tau > 0$. This model is closely related to the full Coulomb model where τ is inversely proportional to the ion velocity, while W_0 is proportional to the charge of the ion [27]. For the best correspondence between the two models we use $\tau = 0.5\hbar/J$ and $W_0 = 8J$. We note that the Gaussian potential is also of practical relevance for experiments with ultracold atoms in optical lattices and allows to simulate ion stopping (for a recent overview, see Ref. [43]).

C. Nonequilibrium Green functions

We compute the correlated time evolution of the lattice electrons, using a nonequilibrium Green functions (NEGF) approach, as described in Ref. [26]. The central quantity is the one-particle Green function [here and in the following we only give the spin-up components (\uparrow) explicitly, the spin-down components follow from replacing $\uparrow \leftrightarrow \downarrow$]

$$G_{ij}^\uparrow(t, t') = -\frac{i}{\hbar} \langle T_C \hat{c}_{i\uparrow}(t) \hat{c}_{j\uparrow}^\dagger(t') \rangle, \quad (4)$$

which is defined as an ensemble average on the Keldysh time contour \mathcal{C} [44], and T_C denotes the contour time-ordering op-

erator. The equations of motion of the greater and less components of the NEGF (4),

$$G_{ij}^{>\uparrow}(t, t') = -\frac{i}{\hbar} \langle \hat{c}_{i\uparrow}(t) \hat{c}_{j\uparrow}^\dagger(t') \rangle, \quad (5)$$

$$G_{ij}^{<\uparrow}(t, t') = \frac{i}{\hbar} \langle \hat{c}_{j\uparrow}^\dagger(t') \hat{c}_{i\uparrow}(t) \rangle,$$

are the two-time Keldysh–Kadanoff–Baym equation (KBE) [20, 21, 34]:

$$\sum_k [i\hbar \partial_t \delta_{ik} - h_{ik}^{\text{HF},\uparrow}(t)] G_{kj}^{\lessgtr,\uparrow}(t, t') = \delta_{\mathcal{C}}(t, t') \delta_{ij} + \sum_k \left\{ \int_{\mathcal{C}} ds \Sigma_{ik}^\uparrow(t, s) G_{kj}^\uparrow(s, t') \right\}^{\lessgtr}. \quad (6)$$

Here, $\delta_{\mathcal{C}}$ denotes the delta function on the contour, and $h_{ij}^{\text{HF},\uparrow}(t)$ is the time-dependent effective one-particle Hamiltonian, which explicitly includes the Hartree contribution to the electron-electron interaction,

$$h_{ij}^{\text{HF},\uparrow}(t) = -\underbrace{J \delta_{\langle i,j \rangle}}_{=J_{ij}} + \left[W_i(t) - i\hbar U(t) G_{ii}^{<\downarrow}(t) \right] \delta_{ij}. \quad (7)$$

On the right-hand side of Eq. (6), the contour integral defines the memory kernel of the KBE, in which $\Sigma_{ij}^\uparrow(t, t')$ denotes the correlation part of the selfenergy [i.e., the mean-field part is excluded as it is contained in Eq. (7)]. Systematic expressions for the selfenergy can be constructed by many-body perturbation theory, e.g., using diagram techniques [21, 45]. Below, we treat the correlation selfenergy Σ in two approximations, which conserve particle number, momentum and energy.

1. Mean field approximation [time-dependent Hartree(-Fock)], here correlation effects are neglected.
2. Second-order Born approximation (SOA),

$$\Sigma_{ij}^{\lessgtr,\uparrow}(t, t') = - (i\hbar)^2 U(t) U(t') \times G_{ij}^{\lessgtr,\uparrow}(t, t') G_{ij}^{\lessgtr,\downarrow}(t, t') G_{ji}^{\lessgtr,\downarrow}(t', t), \quad (8)$$

which includes all irreducible diagrams of second order in the interaction U . We note that the SOA selfenergy is a perturbation theory result and, therefore, becomes less accurate when U increases. In the context of ion-impact simulations on finite graphene clusters, the accuracy of the SOA scheme has been validated in Ref. [27].

A detailed recent overview on different selfenergy approximations and their accuracy can be found in the review by Schlünzen *et al.* [23].

D. G1–G2 scheme

The advantage of NEGF simulations is that they allow to accurately capture electronic correlation effects. At the same

time, NEGF simulations are computationally expensive because the CPU time scales cubically with the number of time steps, $\sim N_t^3$. In the recent publications, Refs. [40] and [46], it was demonstrated that the KBE in combination with the HF-GKBA [39, 47] can be solved highly efficiently within a set of time-local differential equations, bringing the CPU time scaling down to N_t^1 . In this description, the equation of motion for the time-diagonal single-particle Green function becomes [46]

$$i\hbar \frac{d}{dt} G_{ij}^{<,\uparrow}(t) = [h^{\text{HF},\uparrow}(t), G_{ij}^{<,\uparrow}(t)]_{ij} + [I + I^\dagger]_{ij}^\uparrow(t). \quad (9)$$

The information of the selfenergy is included in the correlation part of time-diagonal two-particle Green function \mathcal{G} as

$$\begin{aligned} I_{ij}^\uparrow(t) &= \sum_k \int_{t_0}^t d\bar{t} \left[\Sigma_{ik}^{>,\uparrow}(t, \bar{t}) G_{kj}^{<,\uparrow}(\bar{t}, t) \right. \\ &\quad \left. - \Sigma_{ik}^{<,\uparrow}(t, \bar{t}) G_{kj}^{>,\uparrow}(\bar{t}, t) \right] \\ &= -i\hbar U(t) \mathcal{G}_{ijij}^{\uparrow\downarrow\uparrow\downarrow}(t). \end{aligned} \quad (10)$$

The correlation function \mathcal{G} obeys its own equation of motion, which, for the SOA selfenergy [cf. Eq. (8)], attains the form

$$i\hbar \frac{d}{dt} \mathcal{G}_{ijkl}^{\uparrow\downarrow\uparrow\downarrow}(t) - \left[h_{\uparrow\downarrow}^{(2),\text{HF}}, \mathcal{G}_{ijkl}^{\uparrow\downarrow\uparrow\downarrow} \right]_{ijkl}(t) = \Psi_{ijkl}^{\uparrow\downarrow\uparrow\downarrow}(t), \quad (11)$$

with the two-particle Hartree–Fock (HF) Hamiltonian

$$h_{ijkl,\uparrow\downarrow}^{(2),\text{HF}}(t) = \delta_{jl} h_{ik}^{\text{HF},\uparrow}(t) + \delta_{ik} h_{jl}^{\text{HF},\downarrow}(t), \quad (12)$$

and the two-particle source term

$$\begin{aligned} \Psi_{ijkl}^{\uparrow\downarrow\uparrow\downarrow}(t) &= (i\hbar)^2 U(t) \sum_p \left[G_{ip}^{>,\uparrow}(t) G_{jp}^{<,\downarrow}(t) G_{pk}^{<,\uparrow}(t) G_{pl}^{<,\downarrow}(t) \right. \\ &\quad \left. - G_{ip}^{<,\uparrow}(t) G_{jp}^{<,\downarrow}(t) G_{pk}^{>,\uparrow}(t) G_{pl}^{>,\downarrow}(t) \right]. \end{aligned} \quad (13)$$

The coupled equations (9) and (11) are called the G1–G2 scheme and are closely related to the density-operator formalism [48]. For this work, the equations are propagated with a fourth-order Runge–Kutta integration scheme. From the resulting $G^<$ and \mathcal{G} , we have direct access to the observables of interest, namely the site-resolved densities and double occupation

$$n_{ij}(t) = n_{ij}^\uparrow(t) + n_{ij}^\downarrow(t) = -i\hbar \left[G_{ij}^{<,\uparrow}(t) + G_{ij}^{<,\downarrow}(t) \right], \quad (14)$$

$$d_i(t) = n_{ii}^\uparrow(t) n_{ii}^\downarrow(t) + (i\hbar)^2 \mathcal{G}_{iii}^{\uparrow\downarrow\uparrow\downarrow}(t), \quad (15)$$

where d_i consists of a mean field (first term) and a correlation contribution (second term). Below we will also compute the cluster-averaged doublon number

$$d_{\text{av}}(t) = \frac{1}{L} \sum_i d_i(t). \quad (16)$$

Additional important observables are the total energy of the target,

$$E(t) = E_{\text{kin}}(t) + E_{\text{pot}}(t) + E_{\text{int}}(t), \quad (17)$$

comprising the kinetic, potential and interaction energy contributions:

$$E_{\text{kin}}(t) = -J \sum_{ij} \delta_{\langle i,j \rangle} n_{ji}(t), \quad (18)$$

$$E_{\text{pot}}(t) = \sum_i W_i(t) n_{ii}(t), \quad (19)$$

$$E_{\text{int}}(t) = U(t) \sum_i d_i(t). \quad (20)$$

III. NUMERICAL RESULTS

A. Benchmarks against previous HF-GKBA simulations

When an ion penetrates through the target, the electric potential forces the lattice electrons to accumulate near the impact point. For sufficiently fast projectiles this corresponds to a non-adiabatic excitation, leading to an overall energy gain for the cluster electrons. This behavior is shown in Fig. 2, which gives a general overview of the impact dynamics. The figure depicts the total time evolution of the total energy of the target averaged over the number of lattice sites for the case of a single projectile impact. We compare two finite hexagonal systems containing 24 and 96 sites, respectively. Further, we study the influence of the projectile models presented in Sec. II B. Finally, the effect of the electron–electron interaction in the target is analyzed by comparing results for Hartree–Fock (HF) and second-order Born (SOA) selfenergies.

Let us briefly summarize what we observe in Fig. 2. First, one clearly distinguishes four phases. The first, from $t = 0$ to $\approx 25t_0$ depicts the adiabatic switch-on of correlations, which allows us to start the simulations from an uncorrelated initial state. Thus, around $t = 25t_0$, a correlated initial state is achieved which is crucial for a selfconsistent dynamical treatment of the projectile–target interaction. Note that the small kink in the energy, at $t = 25t_0$, is due to the switch on of the electron–ion interaction which is very small but finite for the chosen initial position of the ion. The second and third phases describe the ion approaching and penetrating through the graphene-flake around $t = 93t_0$. Finally, the fourth phase describes the departure of the ion after traversal of the target. The increased total energy of the lattice corresponds to the projectile’s energy loss, which we cannot measure directly within our description.

The amount of transferred energy depends on the electronic correlations in the target and on the theoretical model: the energy gain of the target is higher for HF results than for SOA, in agreement with earlier studies [26]. If the lattice size is increased, the transferred energy is distributed among a larger number of lattice electrons. As a consequence, the energy gain per lattice site is reduced (compare the dashed and full red lines in the inset).

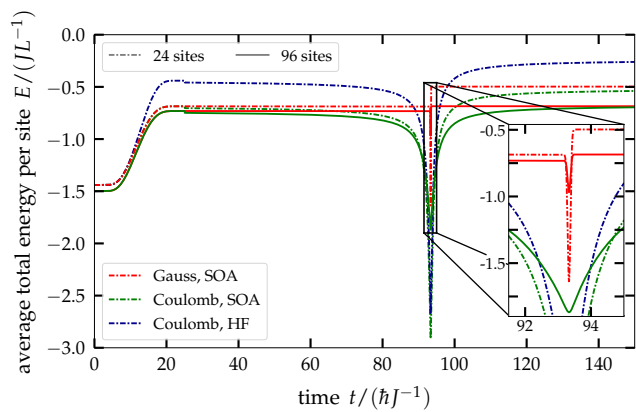


FIG. 2. Average total energy per site of two different lattice sizes, $L = 24$ (dash-dotted lines) and $L = 96$ (solid lines) for a single excitation of the system around $t = 93 t_0$ with $t_0 \approx 0.235\text{fs}$. The three different colors denote different potentials and self energies. For the blue and green curves the Coulomb potential is used to mimic the projectile impact with either time-dependent Hartree-Fock (HF, blue) or second-order Born (SOA, green) as selfenergy approximation. The red curves correspond to an impact mimicked by the Gaussian potential in second-order Born approximation.

Regarding the models of the ionic potential, we observe that—with a suitable choice of parameters—the Gaussian model reproduces the energy gain of the lattice very well (compare the initial and final energies of the red and green curves in phases 2 and 4). However, there are drastic differences during the impact phase. Here the full long-range Coulomb model predicts significantly larger intermediate energy exchange between projectile and target electrons. This is due to the long range of the Coulomb potential, that affects a larger number of lattice charges. This effect is even more pronounced in the case of multiple ion impacts (see Sec. III B). Finally, the increased magnitude of the energy exchange is also important for a proper analysis of the details of the excitation mechanism which involves two-electron excitations and doublon formation [27, 28].

B. Multiple ion impacts. Gauss model vs. Coulomb interaction

When increasing the number of projectiles impacting the honeycomb cluster, a general total energy gain in the lattice can be observed as shown in Fig. 3 (a). It depicts the total energy dynamics of the smallest lattice introduced in Fig. 1 containing $L = 24$ sites. In total, this lattice was excited 20 times ($N_x = 20$) for the Gaussian (red) and the Coulomb (green) potential respectively. Thereby, every peak corresponds to a projectile impact, while the different depths of the peaks can be attributed to the disparate shape and range of the potentials. Both curves describe an ion with charge $Z_p = 1$ with an initial

distance and velocity of

$$\mathbf{r}_{p,0} = - \begin{pmatrix} \frac{1}{6} \\ \frac{\sqrt{3}}{3} \\ 300 \end{pmatrix} a_0, \quad \mathbf{v}_{p,0} = \begin{pmatrix} 0 \\ 0 \\ 3 \end{pmatrix} \frac{a_0}{t_0}, \quad (21)$$

with $t_0 = \frac{\hbar}{J} \approx 0.235\text{fs}$ and $v_{p,0} \approx 1.813 \cdot 10^6\text{m/s}$.

The coordinate $\mathbf{r}_{p,0}$, corresponds to the green point *A* in Fig. 1 and was used as impact point for the Coulomb potential unless stated otherwise. In contrast, the Gaussian potential is directly applied to one of the innermost lattice sites.

Figure 3 (a) shows an initial increase of the total energy un-

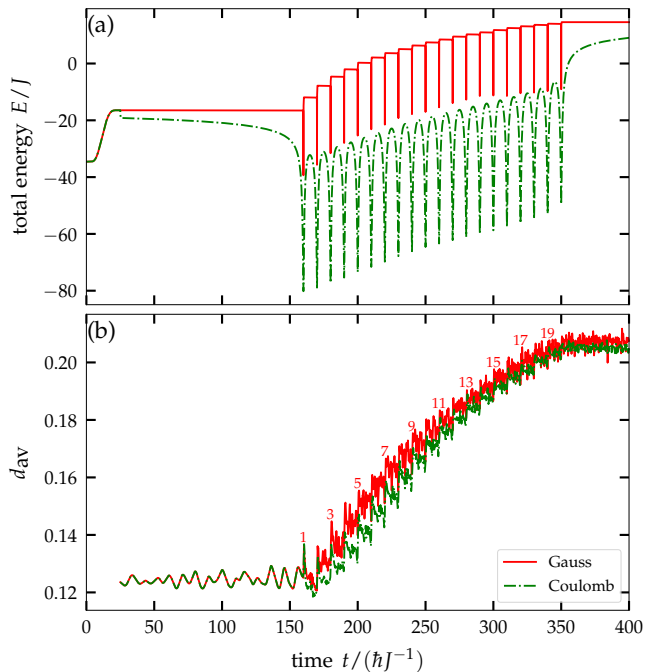


FIG. 3. Top: total energy increase of the lattice containing $L = 24$ sites (cf. Fig. 1) induced by 20 projectile impacts with charge $Z_p e = e$. Comparison of the Gaussian model (red) and the Coulomb interaction potential (green). (b) Cluster averaged doublon number. Numbers in the figure denote the number of the impacting ion. The model details are described in Sec. II B.

til $t = 25 t_0$, which is due to the adiabatic switch-on (AS) of electronic correlations in the solid [23]. After the AS, the respective time-dependent interaction potential with the projectile is turned on. The small kink in the green curve for the total energy at $t = 25 t_0$ is due to the long range of the Coulomb interaction. This kink could be easily eliminated by a different procedure of turning on the projectile-electron interaction, but this would require additional computational cost. When the projectile approaches the cluster plane the total electron energy rapidly decreases and increases again, when the ion leaves. With each new ion this behavior occurs again, in agreement with Fig. 2. Next, we focus on the time evolution of the double occupation, Eq. (16), which is plotted in Fig. 3 (b). We observe that, through multiple periodical excitations, the overall double occupation in the two-dimensional finite clus-

ter can be significantly increased regardless of the potential chosen to mimic the projectile. In the figure, every second excitation is numbered. The instant when an ion passes through the lattice plane is clearly visible from the peaks of d_{av} . If the number of impacts would be increased further, both curves are expected to eventually reach $d_{av} = 0.25$ – the value in an uncorrelated system at half filling, cf. Eq. (15). This is also confirmed by the time evolution of the correlation energy, which steadily decreases with increasing number of excitations.

We now consider a larger system with $L = 96$ sites that is exposed to a further increased number of excitations, $N_x = 40$, the results are presented in Fig. 4. While the overall be-

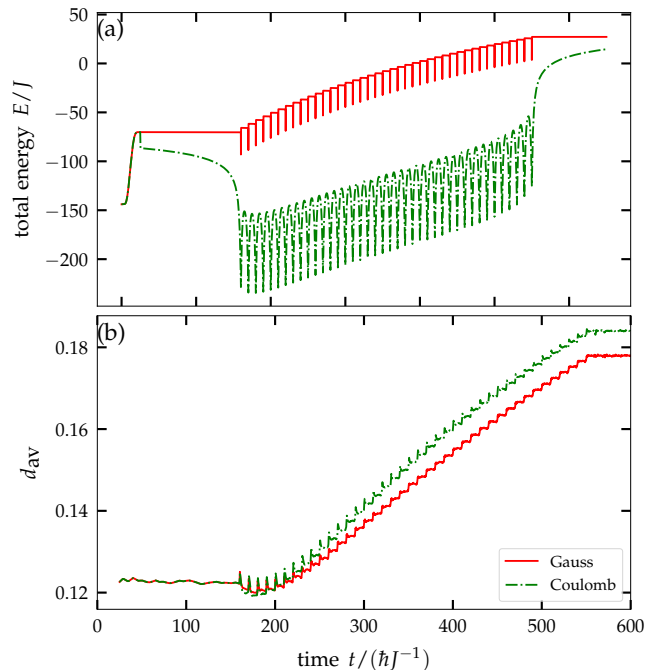


FIG. 4. Total energy (a) and corresponding double occupation increase (b) of the $L = 96$ lattice induced by 40 projectile impacts modelled by a Gaussian potential (red) as well as a Coulomb potential (green). Same input parameters as in Fig. 3.

havior is the same as in Fig. 3, here we observe larger deviations in d_{av} between the Gaussian and Coulomb models, cf. Fig. 4 (b). The reason is the local excitation of a single lattice site, in case of the Gaussian model. With increase of the cluster size a growing number of sites remains unaffected, in contrasted to the long-range Coulomb model.

A novel observation is the slight decrease of the average double occupation during the first few ion impacts. This is observed for both potentials, even though the total energy show different behaviors in the two cases. This effect will be further investigated in the following sections.

C. Dependence of doublon creation on the cluster size

In the following, the effect of the system size on the double occupation dynamics is investigated in more detail.

Fig. 5 shows Coulomb results for lattices of three sizes, $L = 24, 54, 96$. While the overall trend of an increase of the doublon number is observed for all systems, for a larger lattice the increase is slower. The larger the lattice, the more

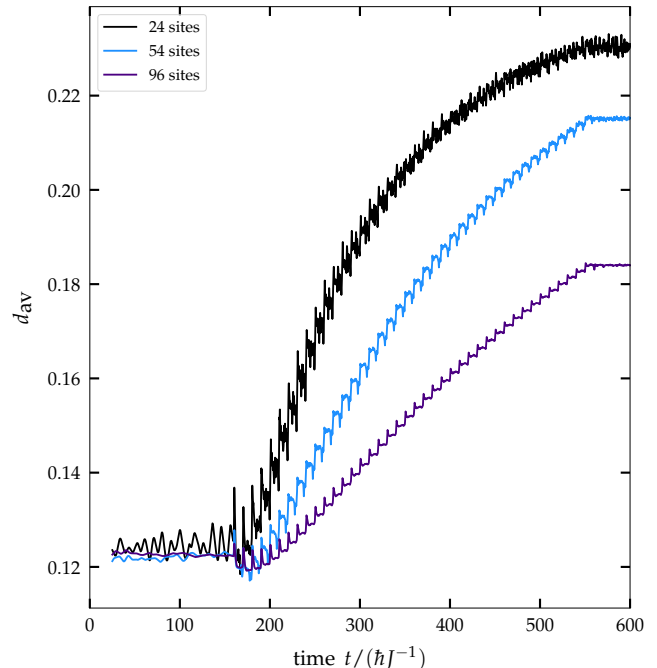


FIG. 5. Cluster averaged double occupation increase through $N_x = 40$ Coulomb excitations for three honeycomb lattice sizes: $L = 24$ (black), $L = 54$ (blue) and $L = 96$ (purple). Same parameters as in Fig. 3.

excitations are needed to reach a specific value for d_{av} , since the projectile energy is shared between a growing number of electrons, in agreement with the observations of Balzer *et al.* [27]. Moreover, for the same reason, the peak height resulting from individual impacts and the noise in between two consecutive excitations is reduced when the lattice grows. Another interesting observation is that the broad global minimum mentioned in the previous section seems to widen for growing cluster sizes. Thus, more excitations are needed to escape that minimum.

We now investigate the asymptotic value of the mean double occupation,

$$d_{av}^{\infty} = \lim_{t \rightarrow \infty} \frac{1}{\Delta t} \int_t^{t+\Delta t} d\bar{t} d_{av}(\bar{t}), \quad (22)$$

which is computed after each excitation. This quantity was analyzed in Ref. [27] for moderate size 1D and 2D honeycomb clusters using HF-GKBA simulations. We now apply the G1–G2 scheme which allows us to extend the analysis to twice as large systems and to larger numbers of excitations. To compare with Ref. [27], we employ the Gaussian potential and use the same input parameters. Overall, the larger systems monotonically continue the trends of the previous results, which is shown in Fig. 6. We also find that the G1–G2 scheme yields

very good agreement with the the previous HF-GKBA results, further comparisons have been made in Ref. [49]. Moreover,

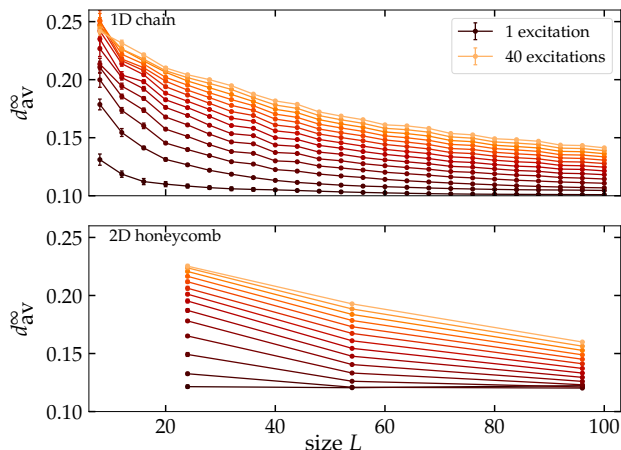


FIG. 6. Asymptotic value of the mean double occupation for 1D chains consisting of up to $L = 100$ sites (top panel) and 2D honeycomb clusters with a maximum of $L = 96$ sites (bottom panel). All systems are excited between one (black curve) and 40 times (light orange) and every third excitation is plotted as a curve. The Gaussian model is used, and the initial values were chosen the same as in Ref. [27].

the previously addressed broad global minimum is observable in the bottom panel at $L = 96$, as the curve of the first excitation yields a higher averaged double occupation than the following, corresponding to $N_x = 4$. This minimum is not visible for the one-dimensional setup. Furthermore, we observe that the 2D setup features a much greater basic level of the averaged double occupation than the 1D one.

The effect of the dimensionality is explored more in detail in Fig. 7 where we compare 1D and 2D clusters containing the same number of sites, $L = 96$. The figure confirms that the broad global minimum of $d_{av}(t)$ does not appear in a linear chain (orange curve), but is restricted to higher dimensionality. Furthermore, the initial double occupation of the honeycomb lattice is significantly larger than the corresponding value of the chain setup and the increase of $d_{av}(t)$ is faster. This is explained by the increased number of nearest neighbors of a lattice site which supports the build-up of correlations.

D. Dependence of doublon creation on the time interval between impacts

We now vary the frequency of ion impacts in a broad range. The results are shown in Fig. 8 for the largest honeycomb cluster ($L = 96$) using the Coulomb potential. The upper panel illustrates how the total energy of the lattice evolves with the number of excitations for the respective impact frequencies. All calculations have been performed for the same total time duration, $t_{max} = 650 t_0$. For this reason, the total energy is much lower for high impact frequencies (green), since there

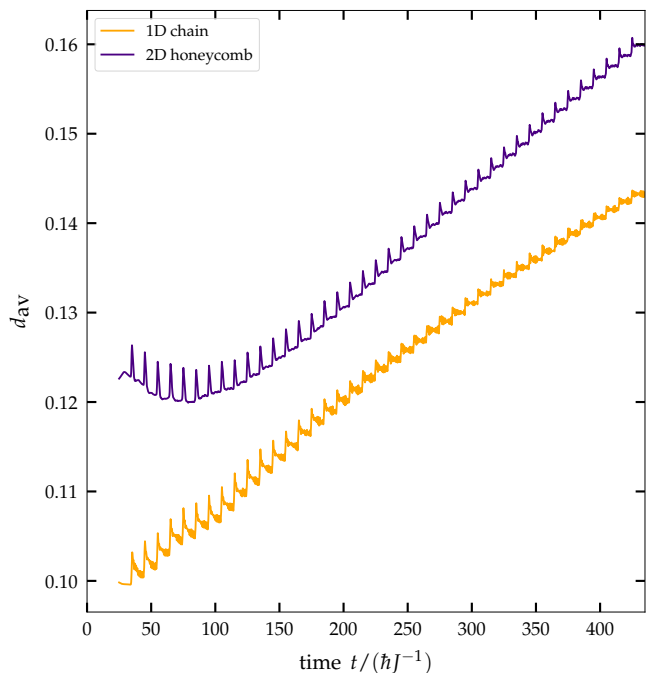


FIG. 7. Cluster averaged double occupation dynamics for the 2D honeycomb lattice (purple) and the 1D chain (orange). Both systems contain $L = 96$ sites and are excited 40 times. The Gaussian potential was used to mimic the projectile, and the input parameters match those of Fig. 6.

are up to twenty times as many excitations compared to the low frequency case, the potentials of which superpose each other. The flattening of the ion-impact peaks in the energy can also be attributed to that superposition, since the interim energy loss of the system directly induced through an impact becomes less relevant with every additional long-range Coulomb potential applied to the lattice electrons. To see the direct influence of the frequency variation, we consider the more sensitive kinetic energy [cf. Eq. (20)] in the middle panel of Fig. 8. Here we see a similar build-up behavior for most time intervals Δt_{imp} , except for the highest ion frequencies, where the energy growth is hampered. For these cases, the ion frequency is on a similar time scale to the immediate electron dynamics in the target. Therefore, the finite correlation spreading and carrier mobility prevent a faster energy transfer.

This effect becomes even clearer for the double occupation (cf. bottom panel of Fig. 8). Again, we observe that for sufficiently large Δt_{imp} , the successive double-occupation build-ups coincide whereas higher frequencies result in a decreased influence per projectile. A peculiarity is found for $\Delta t_{imp} = 10t_0$ (orange curve), for which d_{av} lies slightly below the respective curves for $\Delta t_{imp} = 8t_0$ (blue) and $\Delta t_{imp} = 15t_0$ (red), see the inset of Fig. 8. This non-monotonic behavior can be attributed to an interference of the impact frequency with one of the systems characteristic frequencies and will be further explained in context of Fig. 9.

Another interesting observation is that the broad global minimum of d_{av} vanishes, for very high frequencies. This in-

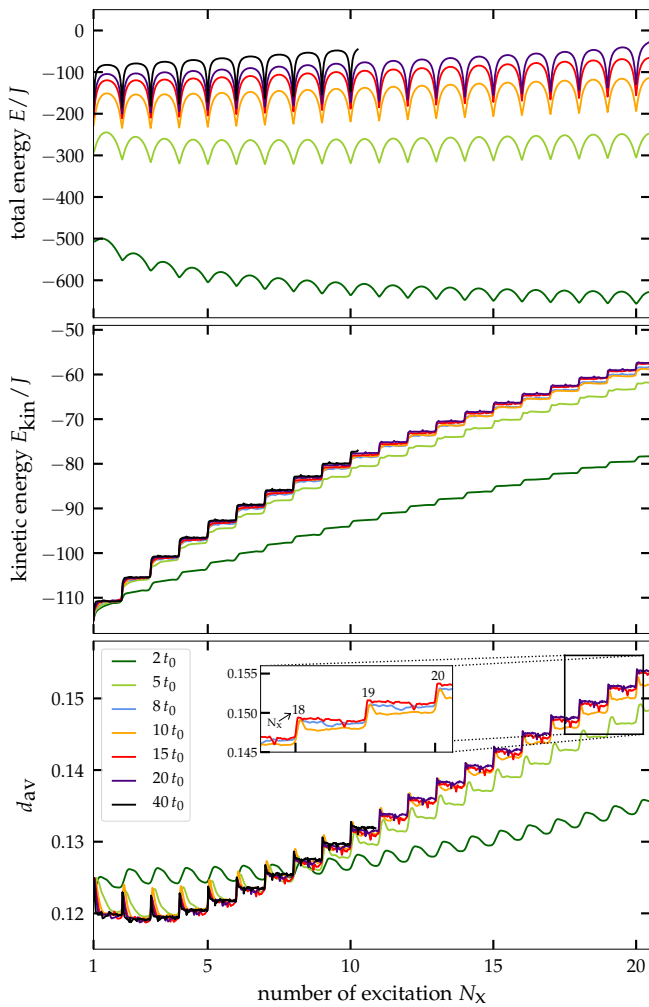


FIG. 8. Dependence of total energy E (top figure) and average double occupation d_{av} (bottom figure) on the number of excitations N_x and the time interval between them, for a 96 sites honeycomb cluster. The six different colors denote different time intervals, Δt_{imp} , in between two consecutive excitations. The orange line ($10 t_0$) corresponds to the interval used in all calculations above. The initial position and velocities of the projectiles match those introduced in Sec. III B.

indicates that the effect is caused by electronic correlation effects on longer time scales. To further investigate the non-monotonic effect in the double occupation, we now focus on the noise in between two excitations and the vibration of d_{av} . In Fig. 9, the time evolution of the average double occupation is shown for different impact frequencies. Obviously, higher frequencies lead to a faster increase of the double occupation, due to the larger number of excitations. Note that, there is a feature that is observed for all impact frequencies: a small kink in d_{av} (upwards for early times and downwards, for later times) appears at approximately $10 t_0$ after each projectile impact. This indicates that there exists a characteristic frequency in the $L = 96$ honeycomb cluster. For $\Delta t_{\text{imp}} = 10 t_0$ (orange), this frequency coincides with the one of the ion impacts. This explains the unusual behavior of the double occu-

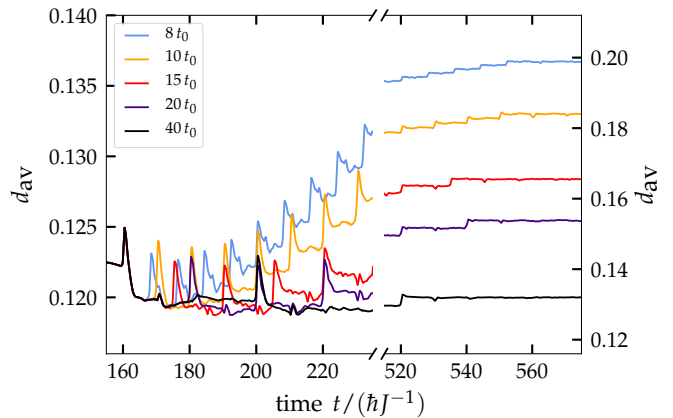


FIG. 9. Cluster averaged double occupation, as shown in Fig. 8, but now plotted versus time. In the right part, the final stage of the time evolution around the final impact is displayed (note the brake of the x-axis).

pation for this case: instead of the small local minima, here maxima are observed.

To find an explanation for the mentioned characteristic frequency of the system, we now investigate the space-resolved carrier redistribution in the lattice.

E. Space-resolved electron dynamics

The highly symmetric 96-site honeycomb cluster consists of four layers of hexagons. To increase the space resolution we consider, instead, seven rings of sites, (sites on the n th ring are those that can be reached from the innermost ring within $n - 1$ steps), cf. Fig. 1. In Fig. 10, we show the time evolution of the average electron density (top) and double occupation (bottom) within each of these rings, following a single ion excitation through the center of the system. For the density, we see a drastic initial increase on the innermost ring that follows from the direct Coulomb attraction by the charged projectile. Simultaneously, the outer rings are slightly depopulated as the electrons move towards the center. Subsequently, we observe a propagating density wave with a finite velocity through the honeycomb rings. For the outer rings, the density change becomes less pronounced, as the electrons spread across a larger number of lattice sites. After a short relaxation phase, the local densities exhibit a second peak (with lower amplitude and opposite sign), although the ion is already far away from the target and no additional excitation is invoked. Thus, the oscillation revival is caused by an intrinsic property of the finite cluster. The time interval between both events is approximately $\Delta t = 10 t_0$, which perfectly agrees with the observed time delay of the energy kinks in Fig. 9. Note that a (less pronounced) second revival is observed after additional $10 t_0$ (cf. the black curve in Fig. 10).

The double occupation (bottom of Fig. 10) exhibits a similar behavior as the density which is explained by the mean field contribution to the doublon number. Note that for the outermost sites, we see a significantly lower double occupation—a

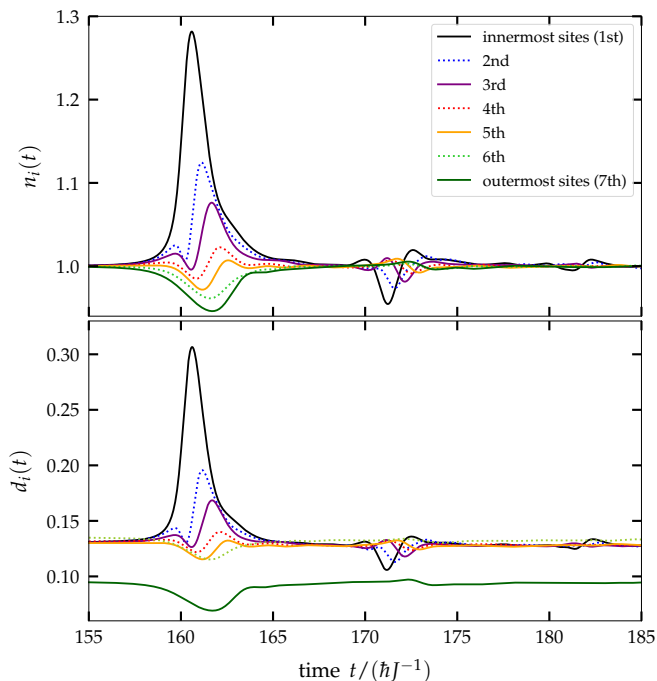


FIG. 10. Time evolution of the local density (top) and double occupation (bottom) on the different honeycomb rings for an ion impact in the center. Due to the highly symmetric setup, the results coincide for all lattice sites of a single ring.

property that is already present in the ground state and at the initial time, due to the reduced connectivity on the edges of the system.

F. Localized versus random impacts

We now consider a different setup where the impact point of the projectiles is varied. To this end, we generate uniformly distributed random positions within a circle of radius $1a_0$. For a fixed time interval of $\Delta t_{\text{imp}} = 10t_0$, we simulate successive ions of the same energy (cf. Eq. (21)) penetrating through those randomized impact points. All computations are performed with a number of $N_x = 50$ excitations. The results are presented in Fig. 11 for the total energy of the lattice (top), the cluster-averaged double occupation (bottom) and the impact positions (right). As a guide to the eye, the innermost hexagon of the 96-site cluster is shown (grey lines). The impact-point distribution is illustrated (purple) alongside of point A in Fig. 1 (orange) and the central position (black). The purple numbers indicate the order of the excitations. From the behavior of the lattice energy and of the double occupation, we conclude that the random impact scenario leads to results that are very similar to the previous findings. In fact, both quantities are predominantly enclosed between the curves for the impact point A (orange) and the central impact (black). Thus, we conclude that the spatially uniform distribution of ion impacts does not significantly change the electronic behavior. A peculiar feature is the random fluctuation of the

energy minima which is caused by the varying distance of the projectile to the nearest lattice sites. At the same time, the average double occupation is not affected by these variations and exhibits the same monotonic trend as for the central impact point (black curve). Furthermore, we recover the broad global minimum, discussed in Sec. III C.

IV. CONCLUSIONS

In summary, we have extended the analysis of electronic correlations, in particular, doublon formation, in small hexagonal graphene-type clusters caused by ion impact, that was presented in a recent Letter [27]. There the scenario of multiple ions hitting the target in the same spot and at fixed time intervals was analyzed, using a nonequilibrium Green functions analysis coupled to an Ehrenfest treatment. The large computational effort of NEGF simulations limited the parameter range that could be studied.

Here, we applied the recently derived G1–G2 scheme [40, 46] to this problem. The advantageous linear scaling with the simulation duration of this approach has allowed us to significantly extend the previous analysis: to larger clusters, to more impacts, as well as to a variation of the impact point and the time interval between impacts. We confirmed that increasing the number of impacts allows to further increase the mean doublon number in the cluster until it eventually approaches the mean field limit 0.25. When the system size is increased the increase of the doublon number slows down since the impact energy is shared among a growing number of electrons. An interesting observation was that, in a 2D hexagonal arrangement of L lattice sites, the average doublon number increases significantly faster compared to a linear arrangement of the sites.

Our fully time-dependent approach is able to resolve non-adiabatic processes in the electronic sub-systems and effects beyond linear response. Non-adiabatic effects are particularly evident at small time intervals between subsequent impacts because the electronic system has not enough time to return to the ground state before the next impact occurs. This can be clearly seen in the behavior of the average double occupation of the electrons shown in Fig. 8. While for large time intervals between projectiles the first few impacts result in a global minimum in the double occupation, the situation changes when the time interval is being reduced. For the interval $5t_0$ only after reaching the global minimum subsequent impacts lead to a periodic but steady increase in the number of doublons, for $2t_0$, this behavior is present from the very first impact and no such minimum can be observed.

We analyzed two protocols of ion impact that can be realized in various experimental setups. First, we studied a strictly periodic sequence of ions that hit the same lattice site; this can be realized with ion guns. Second, we studied a situation where the impact point of the ions is chosen randomly. This case is closer to a gas or a plasma. Interestingly, we observed that the result for the average doublon number is almost the same as in the case of a fixed impact point. What could be done next is to randomly sample the time interval between

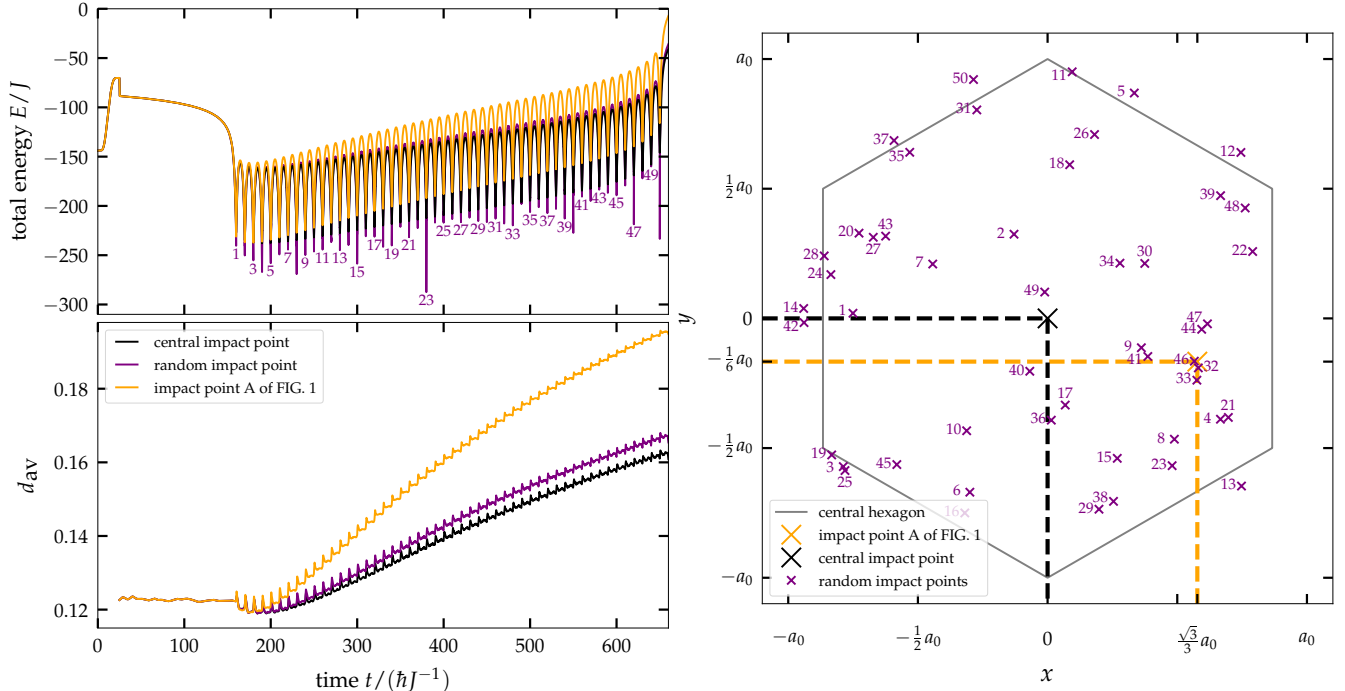


FIG. 11. Response of a 96 site lattice to 50 excitations for three different selections of impact points (sketched in the right figure): black line: central impact; yellow: fixed impact point as in Fig. 1; purple: random impact points, uniformly distributed within a radius of $1a_0$. **Top left:** time evolution of total energy of the lattice E and **bottom left:** time evolution of average double occupation d_{av} – the realized 50 impact points shown in the right panel are numbered in chronological order. The projectiles’ initial velocity is the same as in Fig. 3.

ions as well in order to properly reflect the ion velocity distribution in the gas or plasma. This will allow to make quantitative predictions for the interaction of plasmas with solids, e.g. Ref. [50].

Additional questions that are of interest in the context of ion-solid interaction are innerionic processes such as ion neutralization [32], electronic excitations and secondary electron emission, e.g. Ref. [51]. Such processes have recently become accessible to accurate measurements for highly charged projectiles impacting graphene and other correlated 2D materials, e.g. Refs. [52, 53], and are still missing a full theoretical

description. The present NEGF approach within the G1–G2 scheme provides the proper starting point for this problem as it allows to resolve the full dynamics of electronic correlations. At the same time, the present Hubbard model needs to be extended to include additional bands [16].

ACKNOWLEDGMENTS

We thank Karsten Balzer for helpful discussions.

-
- [1] P. Sigmund, *Particle Penetration and Radiation Effects: General Aspects and Stopping of Swift Point Charges*, Springer Series in Solid-State Sciences (Springer Berlin Heidelberg, 2006).
 - [2] I. Nagy and B. Apagyí, Scattering-theory formulation of stopping powers of a solid target for protons and antiprotons with velocity-dependent screening, *Phys. Rev. A* **58**, R1653 (1998).
 - [3] J. M. Pitarke, R. H. Ritchie, and P. M. Echenique, Quadratic response theory of the energy loss of charged particles in an electron gas, *Phys. Rev. B* **52**, 13883 (1995).
 - [4] P. M. Echenique, R. M. Nieminen, J. C. Ashley, and R. H. Ritchie, Nonlinear stopping power of an electron gas for slow ions, *Phys. Rev. A* **33**, 897 (1986).
 - [5] T. Dornheim, J. Vorberger, and M. Bonitz, Nonlinear Electronic Density Response in Warm Dense Matter, *Phys. Rev. Lett.* **125**, 085001 (2020).
 - [6] M. Quijada, A. G. Borisov, I. Nagy, R. D. Muiño, and P. M. Echenique, Time-dependent density-functional calculation of the stopping power for protons and antiprotons in metals, *Phys. Rev. A* **75**, 042902 (2007).
 - [7] M. A. Zeb, J. Kohanoff, D. Sánchez-Portal, A. Arnau, J. I. Juaristi, and E. Artacho, Electronic Stopping Power in Gold: The Role of d Electrons and the H/He Anomaly, *Phys. Rev. Lett.* **108**, 225504 (2012).
 - [8] A. Schleife, Y. Kanai, and A. A. Correa, Accurate atomistic first-principles calculations of electronic stopping, *Phys. Rev. B* **91**, 014306 (2015).
 - [9] A. Ojanperä, A. V. Krasheninnikov, and M. Puska, Electronic stopping power from first-principles calculations with account for core electron excitations and projectile ionization, *Phys. Rev. B* **89**, 035120 (2014).

- [10] S. Zhao, W. Kang, J. Xue, X. Zhang, and P. Zhang, Comparison of electronic energy loss in graphene and BN sheet by means of time-dependent density functional theory, *Journal of Physics: Condensed Matter* **27**, 025401 (2014).
- [11] S. Bubin, B. Wang, S. Pantelides, and K. Varga, Simulation of high-energy ion collisions with graphene fragments, *Phys. Rev. B* **85**, 235435 (2012).
- [12] F. Mao, C. Zhang, C.-Z. Gao, J. Dai, and F.-S. Zhang, The effects of electron transfer on the energy loss of slow He^{2+} , C^{2+} , and C^{4+} ions penetrating a graphene fragment, *Journal of Physics: Condensed Matter* **26**, 085402 (2014).
- [13] R. Ullah, F. Corsetti, D. Sánchez-Portal, and E. Artacho, Electronic stopping power in a narrow band gap semiconductor from first principles, *Phys. Rev. B* **91**, 125203 (2015).
- [14] J. M. Pruneda, D. Sánchez-Portal, A. Arnau, J. I. Juaristi, and E. Artacho, Electronic Stopping Power in LiF from First Principles, *Phys. Rev. Lett.* **99**, 235501 (2007).
- [15] M. A. Zeb, J. Kohanoff, D. Sánchez-Portal, and E. Artacho, Electronic stopping power of H and He in Al and LiF from first principles, *Nuclear Instruments and Methods in Physics Research Section B: Beam Interactions with Materials and Atoms* **303**, 59 (2013), proceedings of the 11th Computer Simulation of Radiation Effects in Solids (COSIRES) Conference Santa Fe, New Mexico, USA, July 24-29, 2012.
- [16] A. Kononov and A. Schleife, Anomalous stopping and charge transfer in proton-irradiated graphene, *Nano Letters* **21**, 4816 (2021), pMID: 34032428, <https://doi.org/10.1021/acs.nanolett.1c01416>.
- [17] J. F. Ziegler, M. Ziegler, and J. Biersack, SRIM – The stopping and range of ions in matter (2010), *Nuclear Instruments and Methods in Physics Research Section B: Beam Interactions with Materials and Atoms* **268**, 1818 (2010), 19th International Conference on Ion Beam Analysis.
- [18] V. I. Anisimov, F. Aryasetiawan, and A. I. Lichtenstein, First-principles calculations of the electronic structure and spectra of strongly correlated systems: the LDA+ U method, *Journal of Physics: Condensed Matter* **9**, 767 (1997).
- [19] R. Singla, G. Cotugno, S. Kaiser, M. Först, M. Mitrano, H. Y. Liu, A. Cartella, C. Manzoni, H. Okamoto, T. Hasegawa, S. R. Clark, D. Jaksch, and A. Cavalleri, THz-Frequency Modulation of the Hubbard U in an Organic Mott Insulator, *Phys. Rev. Lett.* **115**, 187401 (2015).
- [20] L. Kadanoff and G. Baym, *Quantum Statistical Mechanics* (New York: Benjamin, 1962).
- [21] G. Stefanucci and R. van Leeuwen, *Nonequilibrium Many-Body Theory of Quantum Systems* (Cambridge: Cambridge University Press, 2013).
- [22] K. Balzer and M. Bonitz, *Nonequilibrium Green's Functions Approach to Inhomogeneous Systems* (Springer, Berlin Heidelberg, 2013).
- [23] N. Schlünzen, S. Hermanns, M. Scharnke, and M. Bonitz, Ultrafast dynamics of strongly correlated fermions – Nonequilibrium Green functions and selfenergy approximations, *Journal of Physics: Condensed Matter* **32**, 103001 (2020).
- [24] N. Schlünzen, S. Hermanns, M. Bonitz, and C. Verdozzi, Dynamics of strongly correlated fermions: *Ab initio* results for two and three dimensions, *Phys. Rev. B* **93**, 035107 (2016).
- [25] N. Schlünzen, J.-P. Joost, F. Heidrich-Meisner, and M. Bonitz, Nonequilibrium dynamics in the one-dimensional Fermi-Hubbard model: Comparison of the nonequilibrium Green-functions approach and the density matrix renormalization group method, *Phys. Rev. B* **95**, 165139 (2017).
- [26] K. Balzer, N. Schlünzen, and M. Bonitz, Stopping dynamics of ions passing through correlated honeycomb clusters, *Phys. Rev. B* **94**, 245118 (2016).
- [27] K. Balzer, M. R. Rasmussen, N. Schlünzen, J.-P. Joost, and M. Bonitz, Doublon Formation by Ions Impacting a Strongly Correlated Finite Lattice System, *Phys. Rev. Lett.* **121**, 267602 (2018).
- [28] M. Bonitz, K. Balzer, N. Schlünzen, M. Rasmussen, and J.-P. Joost, Ion impact induced ultrafast electron dynamics in correlated materials and finite graphene clusters, *Phys. Status Solidi B* **257**, 1800490 (2019).
- [29] N. Schlünzen, K. Balzer, M. Bonitz, L. Deuchler, and E. Pehlke, Time-dependent simulation of ion stopping: charge transfer and electronic excitations, *Contrib. Plasma Phys.* **59**, e201800184 (2019).
- [30] F. Aumayr, A. El-Said, and W. Meissl, Nano-sized surface modifications induced by the impact of slow highly charged ions – a first review, *Nuclear Instruments and Methods in Physics Research Section B: Beam Interactions with Materials and Atoms* **266**, 2729 (2008), radiation Effects in Insulators.
- [31] E. Gruber, R. A. Wilhelm, R. Pétuya, V. Smejkal, R. Kozubek, A. Hierzenberger, B. C. Bayer, I. Aldazabal, A. K. Kazansky, F. Libisch, A. V. Krashennnikov, M. Schleberger, S. Facsko, A. G. Borisov, A. Arnau, and F. Aumayr, Ultrafast electronic response of graphene to a strong and localized electric field, *Nature Communications* **7**, 13948 (2016).
- [32] K. Balzer and M. Bonitz, Neutralization dynamics of slow highly charged ions passing through graphene nanoflakes - an embedding self-energy approach, *Contrib. Plasma Phys.* **61**, e202100040 (2021).
- [33] N. E. Dahlen and R. van Leeuwen, Solving the Kadanoff-Baym Equations for Inhomogeneous Systems: Application to Atoms and Molecules, *Phys. Rev. Lett.* **98**, 153004 (2007).
- [34] A. Stan, N. E. Dahlen, and R. van Leeuwen, Time propagation of the Kadanoff–Baym equations for inhomogeneous systems, *J. Chem. Phys.* **130**, 224101 (2009).
- [35] K. Balzer, S. Bauch, and M. Bonitz, Efficient grid-based method in nonequilibrium Green's function calculations: Application to model atoms and molecules, *Phys. Rev. A* **81**, 022510 (2010).
- [36] K. Balzer, S. Bauch, and M. Bonitz, Time-dependent second-order Born calculations for model atoms and molecules in strong laser fields, *Phys. Rev. A* **82**, 033427 (2010).
- [37] M. Garny and M. M. Müller, Quantum boltzmann equations in the early universe, in *High Performance Computing in Science and Engineering, Garching/Munich 2009*, edited by S. Wagner, M. Steinmetz, A. Bode, and M. M. Müller (Springer, Berlin, Heidelberg, 2010) pp. 463–474.
- [38] S. Latini, E. Peretto, A.-M. Uimonen, R. van Leeuwen, and G. Stefanucci, Charge dynamics in molecular junctions: Nonequilibrium Green's function approach made fast, *Phys. Rev. B* **89**, 075306 (2014).
- [39] S. Hermanns, N. Schlünzen, and M. Bonitz, Hubbard nanoclusters far from equilibrium, *Phys. Rev. B* **90**, 125111 (2014).
- [40] N. Schlünzen, J.-P. Joost, and M. Bonitz, Achieving the Scaling Limit for Nonequilibrium Green Functions Simulations, *Phys. Rev. Lett.* **124**, 076601 (2020).
- [41] M. I. Katsnelson, *Graphene: Carbon in Two Dimensions* (Cambridge University Press, 2012).
- [42] M. Schüler, M. Rösner, T. O. Wehling, A. I. Lichtenstein, and M. I. Katsnelson, Optimal Hubbard Models for Materials with Nonlocal Coulomb Interactions: Graphene, Silicene, and Benzene, *Phys. Rev. Lett.* **111**, 036601 (2013).
- [43] C. Gross and I. Bloch, Quantum simulations with ultracold atoms in optical lattices, *Science* **357**, 995 (2017).

- [44] L. Keldysh, Diagram technique for nonequilibrium processes, Soviet Phys. JETP **20**, 1018 (1965), (Zh. Eksp. Teor. Fiz. **47**, 1515 (1964)).
- [45] N. Schlünzen and M. Bonitz, Nonequilibrium Green Functions Approach to Strongly Correlated Fermions in Lattice Systems, Contrib. Plasma Phys. **56**, 5 (2016).
- [46] J.-P. Joost, N. Schlünzen, and M. Bonitz, G1-G2 scheme: Dramatic acceleration of nonequilibrium Green functions simulations within the Hartree-Fock generalized Kadanoff-Baym ansatz, Phys. Rev. B **101**, 245101 (2020).
- [47] P. Lipavský, V. Špička, and B. Velický, Generalized Kadanoff-Baym ansatz for deriving quantum transport equations, Phys. Rev. B **34**, 6933.
- [48] M. Bonitz, *Quantum Kinetic Theory*, 2nd ed., Teubner-Texte zur Physik (Springer, Cham, 2016).
- [49] L. Borkowski, *Electronic Correlations in Lattice Systems Induced by Multiple Ion Impacts: A Nonequilibrium Description via the G1-G2 Scheme*, Bachelor thesis, Christian-Albrechts-Universität zu Kiel (2021).
- [50] M. Bonitz, A. Filinov, J.-W. Abraham, K. Balzer, H. Kählert, E. Pehlke, F. X. Bronold, M. Pamperin, M. Becker, D. Löffhagen, and H. Fehske, Towards an integrated modeling of the plasma-solid interface, Frontiers of Chemical Science and Engineering **13**, 201 (2019).
- [51] M. Pamperin, F. X. Bronold, and H. Fehske, Many-body theory of the neutralization of strontium ions on gold surfaces, Phys. Rev. B **91**, 035440 (2015).
- [52] R. A. Wilhelm, E. Gruber, J. Schwestka, R. Kozubek, T. I. Madeira, J. P. Marques, J. Kobus, A. V. Krasheninnikov, M. Schleberger, and F. Aumayr, Interatomic coulombic decay: The mechanism for rapid deexcitation of hollow atoms, Phys. Rev. Lett. **119**, 103401 (2017).
- [53] A. Niggas, S. Creutzburg, J. Schwestka, B. Wöckinger, T. Gupta, P. Grande, D. Eder, J. Marques, B. Bayer, F. Aumayr, R. Bennett, and R. Wilhelm, Peeling graphite layer by layer reveals the charge exchange dynamics of ions inside a solid, Commun. Phys. **4**, 180 (2021).